

# Electrochemical performance of carbon-supported Pt(Cu)

## electrocatalysts for low-temperature fuel cells

Julia Garcia-Cardona<sup>a</sup>, Ignasi Sirés<sup>a</sup>, Francisco Alcaide<sup>a,b</sup>, Enric Brillas<sup>a</sup>,  
Francesc Centellas<sup>a</sup>, Pere L. Cabot<sup>a,\*</sup>

<sup>a</sup> *Laboratori d'Electroquímica dels Materials i del Medi Ambient, Departament de Química Física, Facultat de Química, Universitat de Barcelona, Martí i Franquès 1-11, 08028 Barcelona, Spain*

<sup>b</sup> *CIDETEC, Paseo Miramón, 196, 20014 Donostia-San Sebastián, Spain (permanent address)*

\*Author for correspondence: Tel: (+34) 934039236, Fax: (+34) 934021221, E-mail address: p.cabot@ub.edu (Pere L. Cabot).

## ABSTRACT

Pt(Cu) nanoparticles supported on carbon nanofibers (CNFs), multi-walled carbon nanotubes (MWCNTs) and Vulcan carbon XC72, have been synthesized by electroless deposition and galvanic exchange. The structural analyses show contracted Pt fcc lattices due to the formation of a PtCu alloy core covered by a Pt-rich shell, mean crystallite sizes of about 3 nm, as well as good dispersion and carbon attachment. The electrochemical surface areas (ECSAs) of Pt(Cu)/CNF and Pt(Cu)/XC72 are comparable to those of commercial Pt/C and PtCu/C. The Pt(Cu) electrocatalysts show more negative onset potentials for CO oxidation than Pt/C and PtCu/C, thus indicating their greater CO tolerance. Pt(Cu)/CNF and Pt(Cu)/MWCNT present the highest mass activity and specific activity for the O<sub>2</sub> reduction, respectively, both with better relative stability than Pt(Cu)/XC72. Pt(Cu)/CNF and Pt(Cu)/MWCNT are then considered good cathode catalysts, yielding estimated savings of about 50 wt.% Pt, when applied to low-temperature fuel cells.

*Keywords:* CO oxidation; galvanic exchange; low-temperature fuel cells; oxygen reduction reaction; Pt(Cu) electrocatalysts.

## 1. Introduction

The energy demand has increased considerably in recent years and the needs have been mainly fulfilled by using fossil fuels, which are rapidly depleting and cause a huge impact on the environment because of the emission of greenhouse gases and pollutants, thereby contributing to the climate change, health problems and acid rain [1-3]. Therefore, it is mandatory to increase the use and development of renewable energy. Fuel cells are one of the most promising green alternatives because they can operate more efficiently than other energy sources, being only dependent on an unlimited renewable source of reactants and approaching zero carbon emissions [4].

It is well known that a large part of the greenhouse gas emissions and release of atmospheric pollutants arises from the use of fossil fuels for transportation. The proton exchange membrane fuel cells (PEMFCs) represent a big advantage over internal combustion engines in automotive vehicles, as they produce zero emissions when using hydrogen as the fuel and oxygen from the air as the oxidant [2,5]. In PEMFCs, the catalysts are generally based on Pt, which is the best material to promote the hydrogen oxidation reaction (HOR) and the oxygen reduction reaction (ORR). However, this metal is too expensive and scarce on the Earth and, moreover, when used at the anode in PEMFCs, it can be easily poisoned by the CO impurities contained in the H<sub>2</sub> gas of industrial grade [6]. To counteract this problem, the use of PtRu electrocatalysts has been proposed [7–9], but the high price of Ru is still a major drawback.

As a strategy to economize Pt, the synthesis of carbon-supported multi-metallic catalysts may allow the reduction of the Pt content. Core-shell nanoparticles, in which a Pt shell coats the surface of a sacrificial metal core that is cheaper and/or more abundant [10–12], are particularly interesting among such materials. The structural properties of

the noble catalyst undergo significant changes due to its interactions with the core. The surface stress and changes in the electronic properties of the noble coating can eventually lead to a remarkable improvement of its catalytic properties.

The Pt-Cu bimetallic system is the object of recent interest [11–36]. Cu covered by noble metals without carbon support [11,12] and PtCu alloys, Pt(Cu) core-shells and Cu-dealloyed PtCu supported on carbon blacks [13–30] have been studied to determine their structure and activity in front of CO and methanol oxidation, ethanol oxidation and the oxygen reduction reaction (ORR). Promising results regarding the reduction of Pt amount and CO poisoning have been obtained. These catalysts have been mainly supported on Vulcan carbon XC72 and XC72R using different procedures [14–28]. In aqueous media, the Pt(Cu) core-shell electrocatalysts have been prepared either by direct current deposition [18,23,24] or electroless deposition of Cu using NaBH<sub>4</sub> [19,25], formaldehyde [26] and water-ethylene glycol mixtures with NaBH<sub>4</sub> and ascorbic acid [20,27–31], both methods followed by a galvanic exchange of Cu by Pt.

Most of the Pt-based nanoparticle catalysts for PEMFCs are supported on porous materials with high specific surface area because this allows using a small amount of Pt and obtaining a high dispersion and narrow size distribution of Pt nanoparticles, an important requirement for their high catalytic performance [37]. Carbon blacks are the most employed supports due to their high surface area, electrical conductivity, porosity and low cost [23]. However, they have several disadvantages [37,38] such as the presence of impurities, mainly organo-sulphur groups (that can poison the catalyst) and the existence of deep micropores that can trap the catalyst nanoparticles (thus making them inaccessible to reactants). In addition, carbon blacks are thermochemically unstable and therefore, they can suffer corrosion with the consequent disintegration of the catalyst layer.

Multi-walled carbon nanotubes (MWCNTs) and carbon nanofibers (CNFs) present some advantages as compared to carbon blacks. They exhibit a unique structure and properties that provide high electrical performance and a specific metal-support interaction (between the delocalized  $\pi$ -electrons of the carbon support and Pt d-electrons) [38,39]. In addition, CNTs and CNFs have few impurities, they do not show deep cracks and can enhance the cell performance with their ordered structure, thereby favoring the mass transport and the electron conductivity. The carbon support may be oxidized in the PEMFC cathode, due to the O<sub>2</sub> feed, especially under standby conditions, thus causing the detachment of the Pt nanoparticles with the corresponding activity loss. CNTs have shown to improve the durability of catalysts as compared with Vulcan XC72 [22,39–41]. An accelerated degradation test in diluted acidic solution at high potential (1.2 V vs RHE) has been made to study the durability of both, the support and the supported catalysts. It was observed that the oxygen content in Vulcan XC72 was much higher than that in CNTs, whereas the degradation of the surface area of the Pt nanoparticles was greatly suppressed when supported on the latter, which was attributed to their larger resistance to corrosion. Previous works have studied the synthesis and characterization of Cu-dealloyed PtCu alloys supported on CNTs and multi-walled carbon nanotubes (MWCNTs), showing an enhancement of both, the catalytic activity related to the ORR and the electrochemical surface area [42–44].

Considering all this, the main objective of this work is to synthesize and test Pt(Cu) electrocatalysts, supported on CNFs and MWCNTs, for CO oxidation and ORR. The Pt(Cu)/CNF and Pt(Cu)/MWCNT catalysts have been prepared by electroless deposition of copper on the CNFs and the MWCNTs followed by galvanic exchange with Pt. They have been characterized by means of structural and electrochemical techniques and the corresponding results were compared (*i*) to those obtained with synthesized Pt(Cu)

catalysts supported on carbon XC72 (Pt(Cu)/XC72), prepared in the same manner as Pt(Cu)/CNF and Pt(Cu)/MWCNT, and (ii) to commercial Pt/C and PtCu/C.

## 2. Materials and methods

### 2.1. Reagents

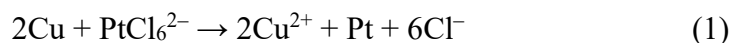
All the reagents were of analytical grade. HNO<sub>3</sub>, NaOH, H<sub>2</sub>SO<sub>4</sub> (98 wt.%), CuSO<sub>4</sub>·5H<sub>2</sub>O, ethanol (96 wt.%) and 2-propanol (dry) were from Panreac. The H<sub>2</sub>PtCl<sub>6</sub> aqueous solution (10 wt.%) was from Merck. NaBH<sub>4</sub> and the Nafion<sup>®</sup> solution (5 wt.%) were from Sigma-Aldrich. The solutions were prepared using Millipore Milli-Q high-purity water (resistivity >18.2 MΩ cm at 25 °C). The carbon supports were Vulcan carbon XC72 from Cabot Corporation and CNFs and MWCNTs from Sigma-Aldrich. The catalysts obtained were compared to Pt/C (20 wt.%) and PtCu/C (1:1, 20 wt.%) commercial catalysts from Premetek, which employ Vulcan XC72 as the carbonaceous support. N<sub>2</sub> and CO gases were Linde 3.0 (purity ≥ 99.9%).

### 2.2. Synthesis of the carbon-supported Pt(Cu) catalysts

The catalysts were prepared following a similar procedure to the two-step synthesis reported by Mintsouli et al. [19], consisting of an electroless deposition of copper ions on the carbon supports followed by partial galvanic replacement of Cu by Pt. The XC72, CNF and MWCNT supports were used as received and also after activation in 2.0 M HNO<sub>3</sub> for 30 min at boiling temperature, the activated specimens being denoted as XC72-A, CNF-A and MWCNT-A, respectively.

First, weighted amounts of CuSO<sub>4</sub>·5H<sub>2</sub>O and the carbon support were dispersed in 1.0 M NaOH using an ultrasonic bath. Then, a determined amount of NaBH<sub>4</sub> was slowly added to stimulate the copper deposition. The sonication was prolonged for 30 min and

then, the suspension was filtered. The powder obtained was resuspended in 0.1 M HCl + 1.5 mM H<sub>2</sub>PtCl<sub>6</sub> using the ultrasonic bath for 45 min to ensure the galvanic replacement according to reaction (1):



which has a standard redox potential of  $E^\circ = 0.404$  V. Finally, the suspension was filtered and the powder was dried at 80 °C. The catalysts thus synthesized were Pt(Cu)/XC72, Pt(Cu)/XC72-A, Pt(Cu)/CNF, Pt(Cu)/CNF-A, Pt(Cu)/MWCNT and Pt(Cu)/MWCNT-A.

### 2.3. Structural characterization

The X-ray diffraction (XRD) of the supports and the catalysts was performed by means of a PANalytical X'Pert PRO MPD  $\theta/\theta$  powder diffractometer (Cu anode, 45 kV, 40 mA), using a Cu K $\alpha$ -filtered radiation ( $\lambda = 1.5418$  Å),  $2\theta$  step size of 0.026° and a measuring time of 200 s per step. The powder samples were sandwiched between films of polyester of 3.6  $\mu\text{m}$  in thickness.

The catalysts were examined by means of transmission electron microscopy (TEM) using a 200 kV JEOL JEM 2100, which also allowed obtaining the corresponding energy-dispersive X-ray spectroscopy (EDS) analyses. In this case, the catalyst powder was sonicated in 3 mL of ethanol for 10 min. A drop of suspension was placed over a holey-carbon Ni grid and then, the solvent was evaporated until total drying using a 40 W lamp for 5 min. For the EDS analyses, about ten different regions of the same sample were examined, taking the corresponding result in composition as the mean value of all of them.

The X-ray photoelectron spectroscopy (XPS) analyses were performed by means of a Physical Electronics PHI 5500 Multitechnique System spectrometer with a

monochromatic X-ray source (Al K $\alpha$  line of 1486.6 eV, powered at 350 W). The energy was calibrated using the 3d<sub>5/2</sub> line of Ag with a full width at half maximum (FWHM) of 0.8 eV. The catalyst powders were disposed on a carbon tape for the analyses. The analyzer was placed 20° with respect to the tape for a better detection of the composition of the external layers. After the initial survey spectrum (187.85 eV of Pass Energy and 0.8 eV/step), the high-resolution spectra (23.5 eV of Pass Energy and 0.1 eV/step) was obtained. The corresponding XPS spectra, acquired without sputtering and after Ar<sup>+</sup> sputtering for 60 s, were analyzed using the MultiPak V8.2B software.

#### *2.4. Electrochemical tests*

The electrochemical characterization of the catalysts was performed in a 200 mL conventional three-electrode cell from Metrohm, provided with a double wall to keep a constant temperature of 25.0  $\pm$  0.1 °C with the help of a Julabo MP-5 thermostat. The reference and auxiliary electrodes were a reversible hydrogen electrode (RHE) from Gaskatel GmbH and a Pt wire, respectively. All the potentials reported in this work are referred to the RHE. The working electrode for the electrochemical tests was a Metrohm glassy carbon (GC) tip (5 mm in diameter, section of 0.196 cm<sup>2</sup>) for Autolab rotating disk electrode (RDE). It was polished with Micropolish II deagglomerated alumina of 0.3 and 0.05  $\mu$ m on a PSA-backed White Felt cloth from Buehler. After each polishing step, the GC was sonicated in water. Suitable amounts of the catalysts were deposited onto the tip of the GC. The catalyst inks were prepared from 1 mg of the catalyst powder, sonicated in 500  $\mu$ L of a mixture of isopropanol and water (1:1 in volume) for 30 min. Volumes of 20  $\mu$ L of the ink were dropped onto the GC tip and, after being dried at room temperature, a thin Nafion<sup>®</sup> film was applied on the catalyst ink. For the cyclic voltammetry (CV) trials, the catalyst was coated with 2.5  $\mu$ L of 5 wt.% Nafion<sup>®</sup> solution, whereas to study the ORR, it was coated with 5  $\mu$ L of 0.1 wt.% Nafion<sup>®</sup> solution.

The electrochemical experiments were performed in 0.50 M H<sub>2</sub>SO<sub>4</sub> using a Solartron SI 1287 potentiostat-galvanostat, commanded by a CorrWare software, version 2.6b. Before the CV tests, N<sub>2</sub> was bubbled for 30 min through the solution in order to remove the dissolved O<sub>2</sub> and it was kept over the liquid surface during these measurements. After the O<sub>2</sub> removal, the working electrode was scanned repeatedly at a scan rate of 100 mV s<sup>-1</sup> within the potential range from 0.0 to 1.2 V until reaching a stationary profile to ensure the removal of any adsorbed impurity. Afterwards, steady cyclic voltammograms were recorded at 20 mV s<sup>-1</sup> within the same potential range. To obtain the CO stripping curves, CO was first bubbled through the solution for 15 min, whereas a potential of 0.1 V was applied to the working electrode. The dissolved CO was removed by N<sub>2</sub> bubbling through the solution for 30 min and then, the adsorbed CO monolayer was oxidized by CV within the range 0.0-1.2 V at 20 mV s<sup>-1</sup>. The ORR was studied using the RDE with the catalyst-coated GC employing a 0.50 M H<sub>2</sub>SO<sub>4</sub> solution, after bubbling pure O<sub>2</sub> through it. The potential was scanned linearly from 0.8 to 0.0 V at 5 mV s<sup>-1</sup> and at different rotational speeds between 500 and 2500 rpm.

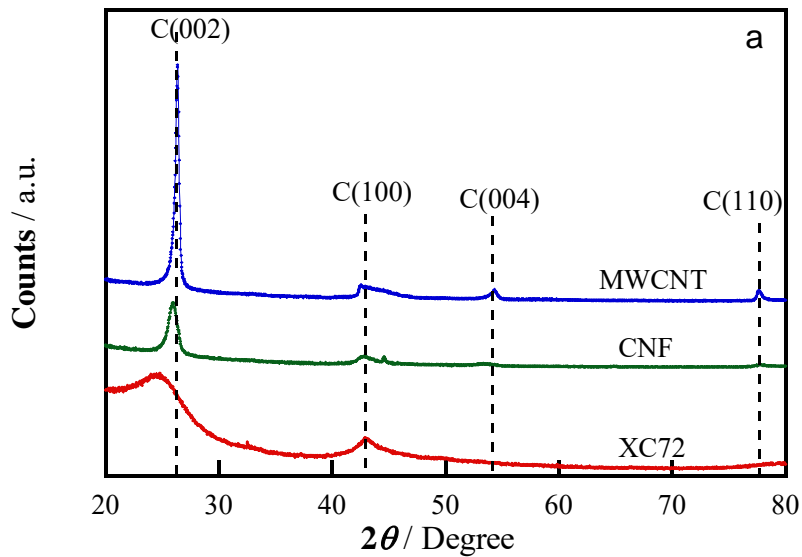
### **3. Results and discussion**

#### *3.1. Structural characterization*

The XRD diffractograms of the different carbon supports are shown in Fig. 1a, where the diffraction lines corresponding to different carbon planes have been highlighted. It is evident that the carbon peak corresponding to the (002) plane at about 26° was much thinner for MWCNTs and CNFs than for Vulcan XC72, suggesting a greater crystallinity of the two former carbons. Although it is not a very relevant factor for the catalyst deposition, the crystallite sizes of the MWCNTs and the CNFs were estimated from that peak using the Scherrer equation:

$$d = \frac{K\lambda}{B \cos \theta} \quad (2)$$

where  $K = 0.9$ ,  $\lambda$  is the wavelength of the X-ray radiation, and  $B$  is the width (in radians) of the measured diffraction peak at an intensity equal to half the maximum intensity. The sizes were thus estimated to be 9.3 and 12 nm for CNFs and MWCNTs, respectively. Considering the C(100) peak, a crystallite size value of 1.3 nm was obtained for XC72. According to the furnishers, the diameter of the CNFs and the MWCNTs was about 100 nm, whereas their lengths were in the range 20-200 and 5-9  $\mu\text{m}$ , respectively. The diameter of the XC72 nearly spherical particles was about 50 nm. The small values of the crystallite sizes with respect to the dimensions of the carbonaceous structures indicate their small range of crystallinity.



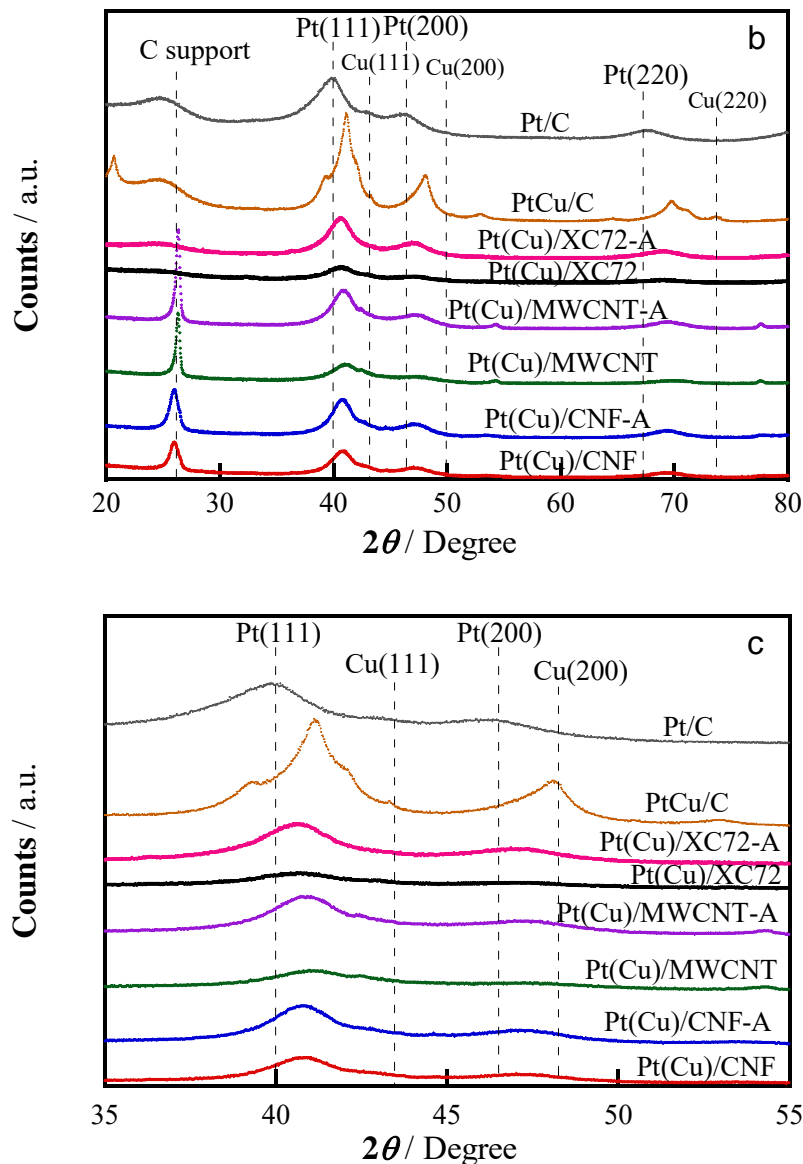


**Fig. 1** – XRD diffractograms of (a) carbon supports and (b) supported catalysts under study. (c) Magnification of the main peaks of plot (b), which correspond to (111) and (200) Pt and Cu planes.

The XRD diffractograms of the different catalysts studied are depicted in Fig. 1b and c. Fig. 1b shows those corresponding to the carbon-supported Pt(Cu) ones, which are compared to those obtained for commercial Pt/C and PtCu/C. The diffractograms of the synthesized ones have all similar shape and Pt appears to predominate. The Cu structure is not clearly identified and no XRD peaks corresponding to copper oxides can be

observed. The XRD peaks of these carbon-supported Pt(Cu) catalysts can be related to fcc Pt (111), (200) and (220) planes and they are located at  $2\theta$  values of  $40.8^\circ$ ,  $47.2^\circ$  and  $69.2^\circ$ , respectively (PDF #00-001-1194) [45]. As shown in Fig. 1b, the Pt peaks corresponding to commercial Pt/C are located at  $40.0^\circ$ ,  $46.3^\circ$  and  $67.5^\circ$ . The shift of the Pt peaks in the synthesized Pt(Cu) samples indicates that a PtCu alloy is probably formed. Shifting to higher angles with respect to pure Pt can be explained by a lattice contraction as a consequence of the formation of the PtCu alloy, because the atomic radius of Cu (145 pm) is smaller than that of Pt (177 pm). The XRD diffractogram of commercial PtCu/C also included in Fig. 1b and c shows diffraction peaks related to those of the three mentioned planes of Pt at  $41.1^\circ$ ,  $48.1^\circ$  and  $69.8^\circ$ , respectively. The diffraction angles of the synthesized carbon-supported Pt(Cu) catalysts are between those of pure Pt and PtCu. Accepting that the Pt signal shift is due to Cu alloying, the Cu content in commercial PtCu should be higher. The composition of the PtCu alloys in the samples studied can be estimated from Vegard's law, which relates the lattice parameter  $a_{\text{PtCu}}$  of the PtCu alloy with the atomic fraction of Cu (x):

$$a_{\text{PtCu}} = (1-x) a_{\text{Pt}} + x a_{\text{Cu}} \quad (3)$$

where  $a_{\text{Pt}}$  and  $a_{\text{Cu}}$  are the lattice parameter of Pt (0.3916 nm) and Cu (0.3608 nm) [45]. The corresponding results are shown in Table 1. As shown in this table, the amount of Pt in the PtCu alloy lattice of the Pt(Cu) catalysts is in the range 1.6-2.7 times greater than that of Cu, whereas that of the commercial one approaches the Pt:Cu 1:1 ratio. This indicates that in the galvanic exchange of Cu by Pt, the external Cu atoms are oxidized and replaced by Pt and that some lattice reordering takes place to form a PtCu alloy, in agreement with previous results in the literature [20,31,32]. If residual Cu oxidized species remained on the catalyst surface, they should be amorphous or in rather small amounts, since no Cu(II) crystalline phases were found in the diffractograms.

As shown in Fig. 1b and c, the Pt diffraction peaks are broad. This peak broadening could be caused, apart from the small size of the nanoparticles, by their non-uniform composition and therefore, the superposition of the peaks of different phases, as previously reported by Guterman et al. [30]. In spite of not being pure metals, the crystallite size of the nanoparticles was estimated from Scherrer's equation (2), with the values also listed in Table 1. Note that these values are around 3 nm, which is considered a suitable size for PEMFCs application.

**Table 1** – Crystallite sizes of the catalyst nanoparticles and PtCu alloying obtained from the XRD diffractograms of Fig. 1 and catalyst composition from EDS analyses.

Catalyst	Crystallite size / nm	Pt:Cu at % ratio <sup>a</sup>	Metal content <sup>b</sup> / wt %		Pt:Cu at % ratio <sup>c</sup>
			Pt	Cu	
Pt(Cu)/CNF	2.9	71:29	5.1	4.1	29:71
Pt(Cu)/CNF-A	2.3	66:34	5.9	6.2	24:76
Pt(Cu)/MWCNT	3.0	62:38	7.4	5.9	29:71
Pt(Cu)/MWCNT-A	2.8	66:34	8.1	6.2	30:70
Pt(Cu)/XC72	2.0	73:27	7.4	7.3	25:75
Pt(Cu)/XC72-A	4.7	70:30	5.7	4.2	31:69
PtCu/C (commercial)	3.4	57:43	15.1	4.9	50:50
Pt/C (commercial)	2.6	100:0	20.0	0.0	100:0

<sup>a</sup> Pt:Cu atomic ratio of the PtCu alloy from XRD (Vegard's law)

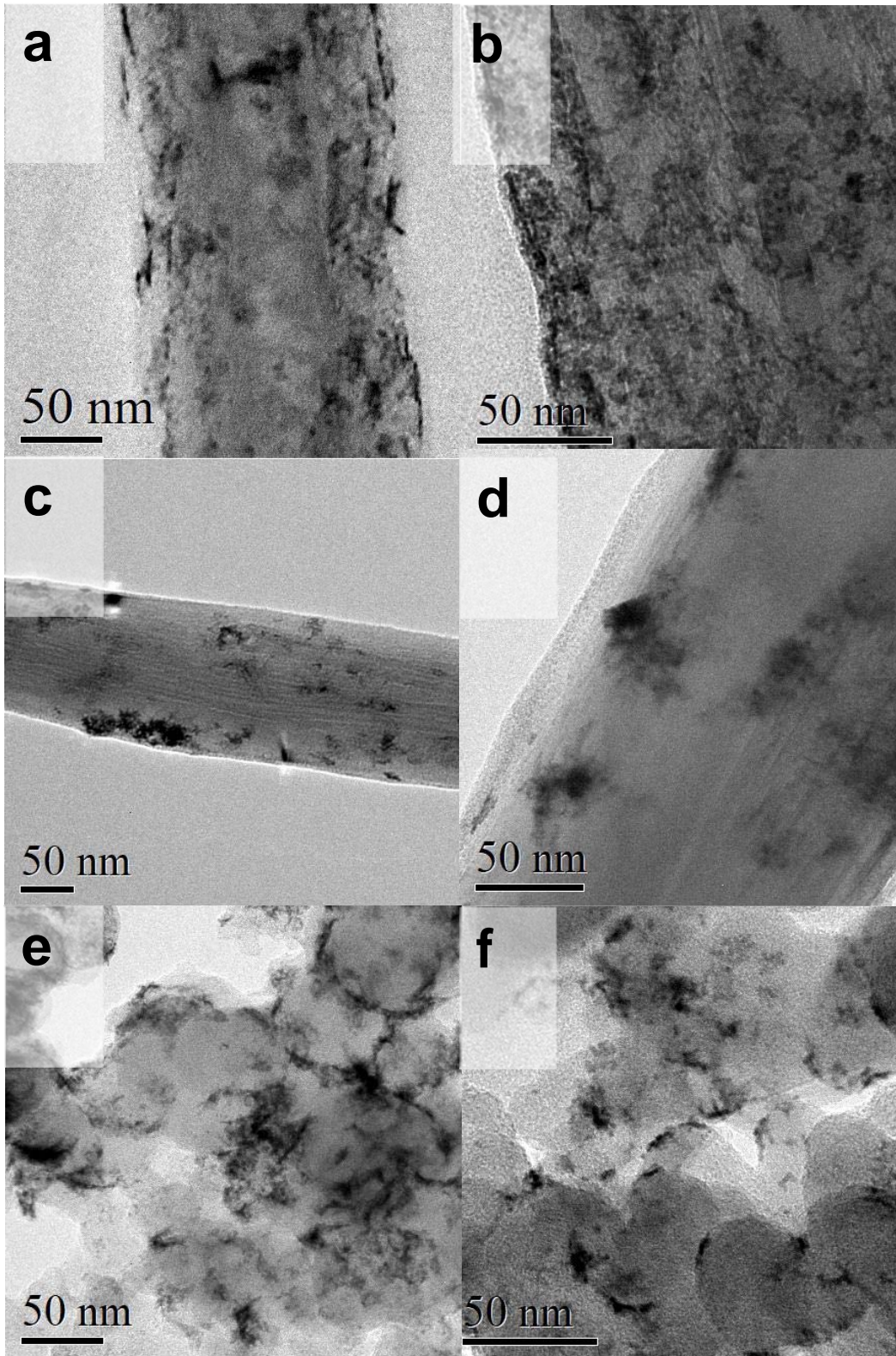
<sup>b</sup> Overall content in the catalyst from EDS (mean standard deviation of 1.5 wt %)

<sup>c</sup> Pt:Cu atomic ratio in the catalyst from EDS

Fig. 2 shows TEM images of the synthesized catalysts, where the Pt(Cu) nanoparticles can be seen as black spots. These images also show the morphology of the carbonaceous supports, displaying the shape of fibers for Pt(Cu)/CNF and Pt(Cu)/CNF-

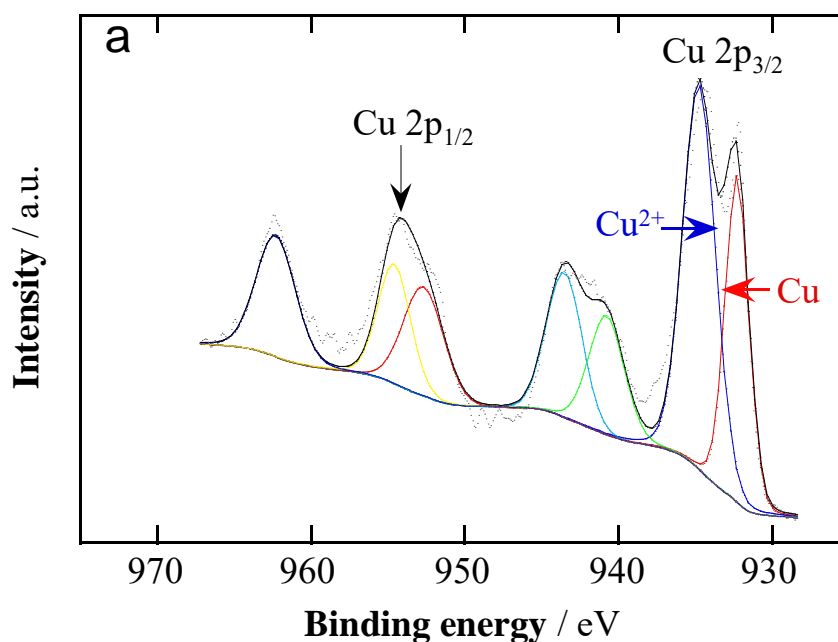
A (Fig. 1a and b, respectively), nanotubes for Pt(Cu)/MWCNT and Pt(Cu)/MWCNT-A (Fig. 1c and d), and spherules for Pt(Cu)/XC72 and Pt(Cu)/XC72-A (Fig. 1 e and f). As shown in these figures, the diameter of the carbonaceous materials and their length in the case of the nanofibers and nanotubes correspond to the values provided by the furnishers, mentioned in the experimental part. The Pt(Cu) nanoparticles appear to be organized in a variety of sizes, with relative dispersion over the supports and some aggregation. There is a clear evidence in these images of the successful attachment of Pt(Cu) nanoparticles to the carbon support both, using the carbonaceous material as received and after activation. It can also be observed in these figures that the deposited Pt(Cu) crystallites have elongated forms, developed over the support, with little vertical growth. The composition of the supported Pt(Cu) nanoparticles was semiquantitatively determined by EDS, obtaining the values summarized in Table 1. These values are the result of the synthesis history, and it is expected that they strongly depend on the support properties. Accordingly, they will also depend on the crystallite size of the previously deposited Cu nanoparticles.

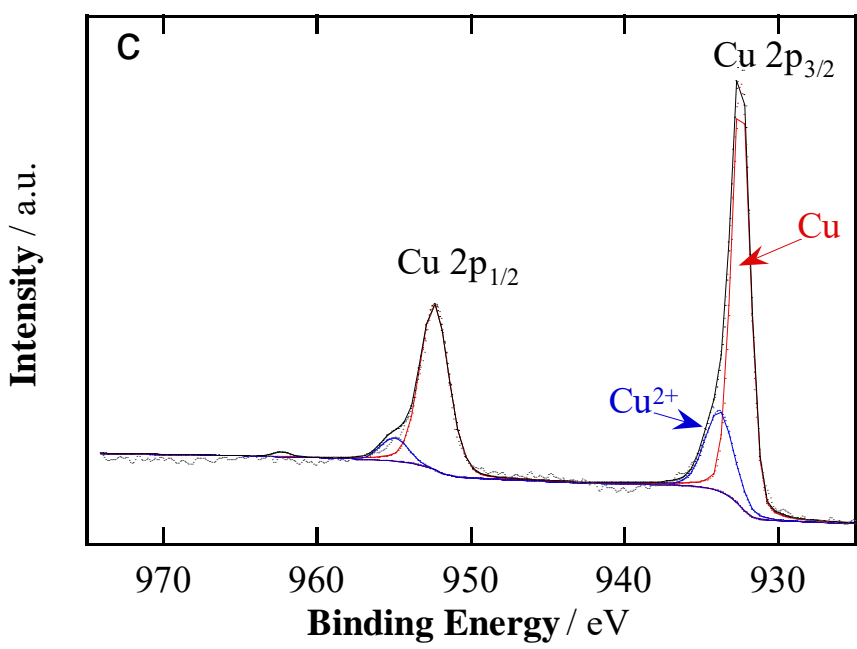
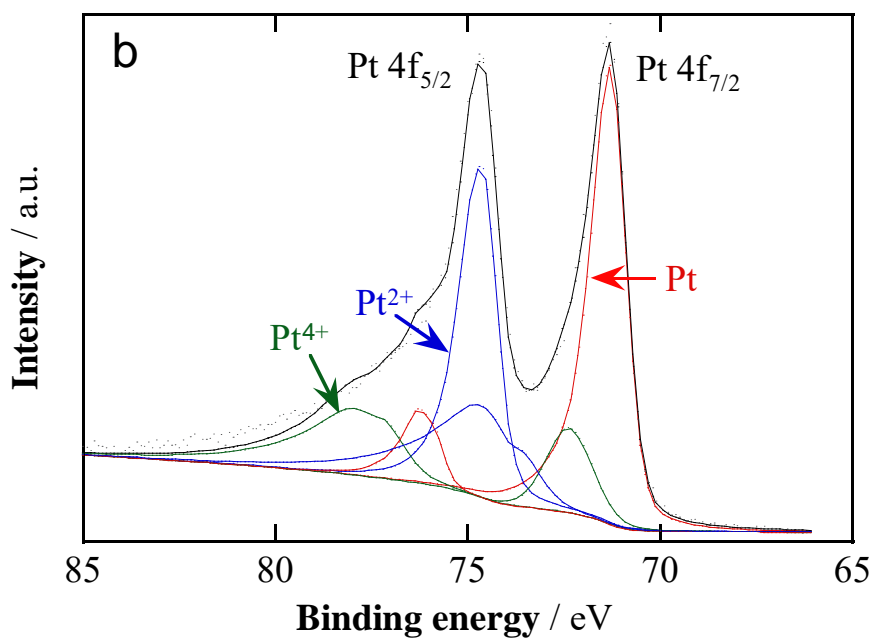
It is interesting to note that the weights of Pt and Cu are in the same order of magnitude, thus indicating that the amount of Pt has been reduced by about 50 wt.%. However, these weights correspond to different atomic amounts of Pt and Cu, the latter being dominant by 2-3 folds. The difference with respect to the PtCu alloy composition obtained from Vegard's law is significant, thus indicating that there many Cu species (oxidized or not) without Pt bonding.



**Fig. 2** - TEM images of (a) Pt(Cu)/CNF, (b) Pt(Cu)/CNF-A, (c) Pt(Cu)/MWCNT, (d) Pt(Cu)/MWCNT-A, (e) Pt(Cu)/XC72 and (f) Pt(Cu)/XC72-A.

EDS line profiles to ascertain the Cu and Pt distribution in the nanoparticles were attempted. However, the resolution was not sufficient because of their small size. For this reason, XPS surface analyses were performed, as suggested by Maya-Cornejo et al [31]. In our case, the spectra were acquired with the analyzer placed  $20^\circ$  with respect to the plane of the samples to obtain a better approach of the composition of the most external layers. No mild sputtering was carried out to avoid the removal of Pt and Cu surface species apart from adventitious carbon. These analyses were performed then without sputtering and with  $\text{Ar}^+$  sputtering for 60 s. The Pt and Cu high resolution spectra measured for Pt(Cu)/CNF are shown in Fig. 3. Fig. 3a and c correspond to the Cu binding energy (BE) region, before sputtering and after sputtering, respectively, and Fig. 3b and d, to the Pt BE region, before sputtering and after sputtering, also respectively. The deconvolution of the spectra revealed the presence of Cu and Pt oxidized species. The atomic percentages of the metallic form with respect to the other forms of the element together with the overall Pt:Cu atomic ratios are listed in Table 2. From these data, the Pt(0):Cu(0) atomic ratio has been derived and also given in the table.





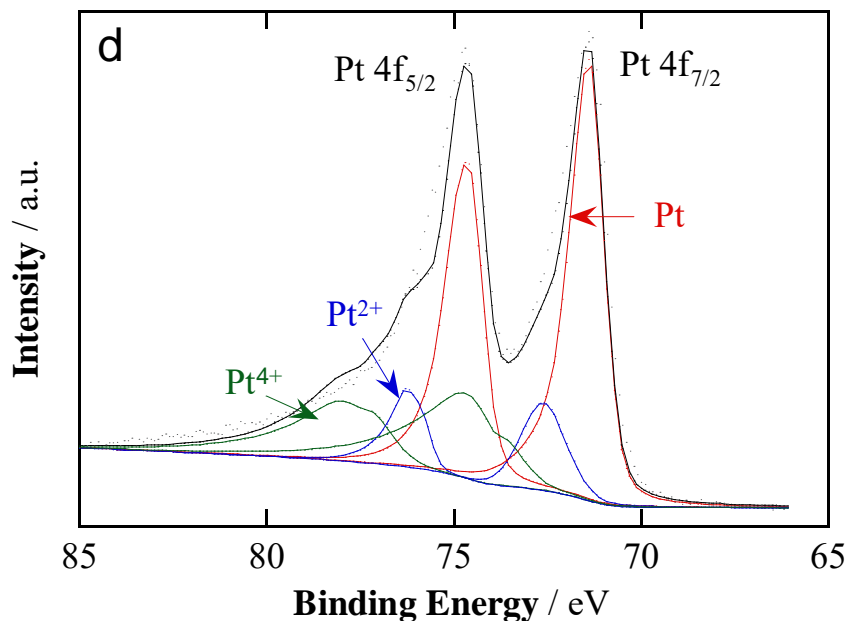


Fig. 3 – Deconvoluted high-resolution XPS spectra of the Pt(Cu)/CNF catalyst in the BE region of Cu: a) before and c) after sputtering; and in the BE region of Pt: b) before and d) after sputtering.

**Table 2** – Relative atomic composition of the different oxidation states of Cu and Pt species in different catalysts. The atomic ratio of the overall forms and of the metallic forms of Pt and Cu is also given.

Species	Ar <sup>+</sup>	Pt(Cu)/CNF	Pt(Cu)/MWCNT	Commercial PtCu/C
Pt(0):Pt(II):Pt(IV)	N	62:10:28	61:17:22	66:11:23
Cu(0):Cu(II)	N	30:70	25:75	43:57
Pt(0):Pt(II):Pt(IV)	Y	66:11:23	50:40:10	43:31:26
Cu(0):Cu(II)	Y	81:19	77:23	72:28
Overall Pt:Cu	N	66:34	57:43	85:15
Overall Pt:Cu	Y	70:30	58:42	76:24
Pt(0):Cu(0)	N	81:19	77:23	90:10
Pt(0):Cu(0)	Y	65:35	48:52	65:35

The data given in Table 2 show for non-sputtered samples the presence of some significant amounts of oxidized Pt and also of big amounts of oxidized copper. It is also shown that oxidized copper largely disappears after Ar<sup>+</sup> sputtering and therefore, it is essentially a residual oxidized copper on the surface. On the other hand, the overall Pt:Cu ratio of the Pt(Cu) catalysts does not significantly vary upon sputtering, whereas the Pt(0):Cu(0) ratio, related to the alloy formation, changes significantly, with a marked decrease of the Pt content in this ratio upon sputtering. This strongly suggests that the surface of the catalyst nanoparticles are Pt-enriched and that they can be visualized as a PtCu alloy core covered by a Pt shell or at least by a Pt-rich shell.

### 3.2. Electrochemical characterization

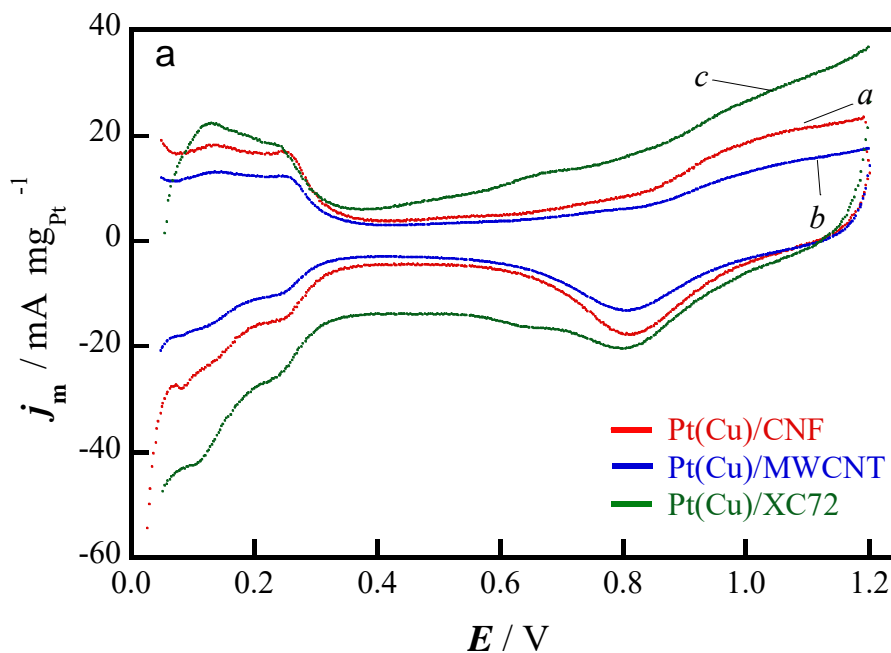
Representative steady cyclic voltammograms of the catalysts under study, using the mass activities  $j_m$  (current values referred to the Pt load), at 20 mV s<sup>-1</sup> in deaerated 0.50 M H<sub>2</sub>SO<sub>4</sub>, are shown in Fig. 4. The  $j_m$  vs  $E$  curves in Fig. 4a correspond to Pt(Cu)/CNF, Pt(Cu)/MWCNT and Pt(Cu)/XC72. The same catalysts prepared from the activated carbonaceous supports had the same shape as those without activation, but they presented smaller current density values. The shape of these cyclic voltammograms were the same as that of Pt and there was no evidence about Cu dissolution because no additional peaks appeared. This indicates that the Pt-rich shell may avoid the oxidation of the internal Cu. The potential region within the range 0.0-0.3 V corresponded to desorption (anodic sweep) and adsorption (cathodic sweep) of atomic hydrogen. These peaks are not as well defined as in the case of a perfect crystal faceting because the Pt structure appears to be conditioned by the Cu alloying [18,46,47]. The Pt oxidation can be identified from potentials around 0.65 V in the anodic sweep, with the corresponding reduction peak in the cathodic sweep at about 0.8 V. The cyclic voltammogram of PtCu/C (Fig. 4b, curve *d*), presents also the same features as that of Pt/C (Fig. 4b, curve *e*), without additional

peaks for Cu dissolution, thus being in agreement with the existence of a Pt-rich shell (Table 2). Note that the currents per mass of the cyclic voltammogram of Pt(Cu)/CNF (Fig. 4a, curve *a*) are close to those of the curves shown in Fig. 4b. Overlapping of these three curves indicates that they have comparable electrochemical surface areas (ECSAs).

The ECSAs of the catalysts were estimated from the hydrogen potential region of the corresponding cyclic voltammograms. The overall charge of hydrogen desorption ( $Q_{\text{H-des}}$ , in  $\mu\text{C}$ ) for a given Pt load ( $g_{\text{Pt}}$ , in  $\mu\text{g}_{\text{Pt}} \text{cm}^{-2}$ ) was determined, and considering that the charge associated with the formation or stripping of an atomic hydrogen monolayer is  $210 \mu\text{C} \cdot \text{cm}^{-2}$  [46], the ECSAs were obtained using equation (4):

$$ECSA = \frac{Q_{\text{H-des}}}{210 g_{\text{Pt}}} \quad (4)$$

The obtained values, collected in Table 3, are about  $70\text{-}80 \text{ m}^2 \text{ g}_{\text{Pt}}^{-1}$  for all the catalysts except for the MWCNTs and those using the activated carbons. Activation is typically performed to increase the number of nucleation centers for the nanoparticles. However, in this case, it did not yield a larger ECSA, probably because there is a larger agglomeration as compared to the non-activated ones and they are then less accessible.



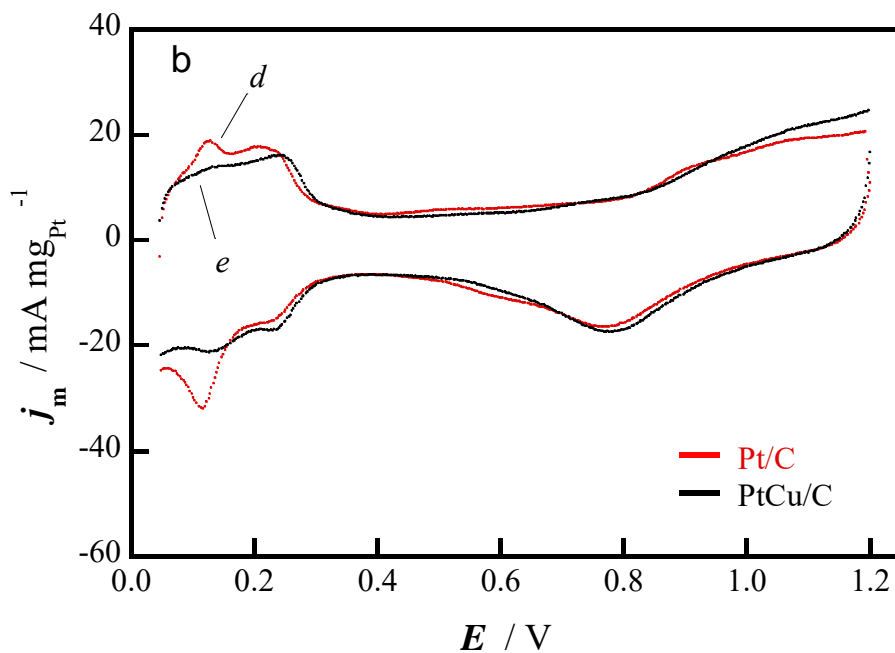


**Fig. 4** – Cyclic voltammograms of the carbon-supported catalysts in deaerated 0.50 M H<sub>2</sub>SO<sub>4</sub> at a scan rate of 20 mVs<sup>-1</sup>. (a) Synthesized Pt(Cu)/CNF (a), Pt(Cu)/MWCNT (b) and Pt(Cu)/XC72 (c). (b) Commercial PtCu/C (d) and Pt/C (e).

**Table 3** – ECSAs of the studied catalysts, estimated from desorption of atomic hydrogen and from CO stripping. The corresponding Pt loadings are also indicated.

Catalyst	Pt loading / $\mu\text{g cm}^{-2}$	ECSA <sub>H-des</sub> / $\text{m}^2 \text{g}_{\text{Pt}}^{-1}$	ECSA <sub>CO-des</sub> / $\text{m}^2 \text{g}_{\text{Pt}}^{-1}$
Pt(Cu)/CNF	10.4	70.1	70.7
Pt(Cu)/CNF-A	12.0	19.6	20.8
Pt(Cu)/MWCNT	15.1	44.6	44.6
Pt(Cu)/MWCNT-A	16.5	10.7	11.3
Pt(Cu)/XC72	15.1	78.4	78.6
Pt(Cu)/XC72-A	11.6	40.8	41.3
PtCu/C (commercial)	18.5	86.4	87.2
Pt/C (commercial)	20.4	73.3	74.5

The cyclic voltammograms corresponding to CO stripping, using also the mass activities  $j_m$ , are shown in Fig. 5. The oxidation peak between about 0.6 and 1.0 V corresponds in all cases to the oxidative stripping of the pre-adsorbed CO monolayer. Note, however, that there is a significant shift of the onset potential for CO oxidation to more negative potentials, from ca. 0.7 V for PtCu/C (curve *c*) and Pt/C (curve *d*) to ca. 0.65V for Pt(Cu)/CNF (curve *a*) and Pt(Cu)/XC72 (curve *b*). This is in agreement with previous work of the authors using Pt(Cu) catalysts prepared by electrodeposition of Cu nanoparticles on Vulcan carbon XC72R and further galvanic exchange with Pt [18,23,24], in which the same shift with respect to Pt/C was found. This can be explained by the Pt-CO bond weakening due to the effect of the Cu alloying, with the consequent increase in the CO oxidation rate [18,26,48]. The Pt-rich shell in these Pt(Cu) catalysts is then more active for CO oxidation, thus meaning that they are more tolerant to CO. Note that the onset potential for CO oxidation on PtCu/C (Fig. 5, curve *c*) is practically the same as that using Pt/C (curve *d*). The main difference as compared to the carbon-supported Pt(Cu) catalysts is that PtCu appears to have more Pt in the external part (see Table 2), being less effective on the Pt-CO bond. The ECSAs of the catalysts were also determined from the CO stripping curves, considering the charge for the CO desorption ( $Q_{\text{CO-des}}$ ) and that the oxidation of a monolayer of adsorbed CO on polycrystalline Pt requires  $420 \mu\text{C}\cdot\text{cm}^{-2}$  [18,46]. The corresponding results are also listed in Table 3, which shows the excellent agreement with the ECSAs obtained from atomic hydrogen desorption.

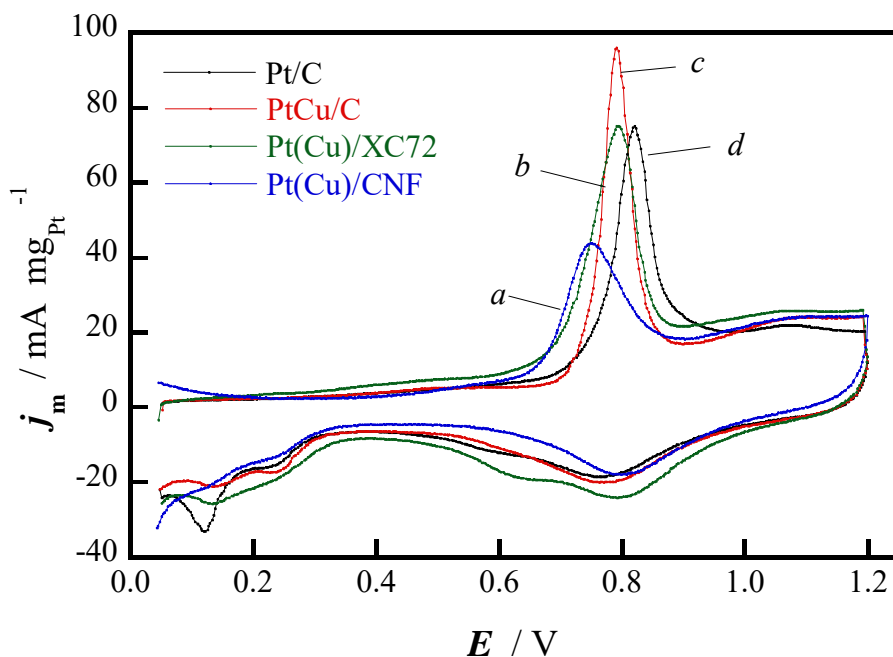


**Fig. 5** – CO stripping curves in deaerated 0.50 M H<sub>2</sub>SO<sub>4</sub> at scan rate of 20 mV s<sup>-1</sup> corresponding to Pt(Cu)/CNF (*a*), Pt(Cu)/XC72 (*b*), PtCu/C (*c*) and Pt/C (*d*).

The catalytic activity of the catalysts in front of the ORR was studied by linear sweep voltammetry in O<sub>2</sub>-saturated 0.50 M H<sub>2</sub>SO<sub>4</sub>, using the RDE. The polarization curves using the mass activities  $j_m$  obtained at a rotational speed of 1500 rpm are shown in Fig. 6a. It is shown that in all cases, the current approaches a limiting value at large overpotentials. The highest  $j_m$  values were obtained using the Pt(Cu)/CNF (curve *a*), followed by the commercial PtCu/C catalyst (curve *d*). According to Fig. 6a, the respective limiting values were about 260 and 180 mA mg<sub>Pt</sub><sup>-1</sup>. Note that the latter is comparable to that obtained for Cu-dealloyed PtCu supported on synthesized CNTs, of about 150 mA mg<sub>Pt</sub><sup>-1</sup>, under the same conditions [44]. There were no significant differences between Pt(Cu)/MWCNT (curve *b*), Pt(Cu)/XC72 (curve *c*) and the commercial Pt/C (curve *e*). Note however, that the onset potential for Pt(Cu)/MWCNT (and also for Pt(Cu)/MWCNT-A) were more positive than those of the other catalysts.

This should entail a greater activity, which is not reflected in the limiting currents per mass, probably because its ECSA is smaller (Table 3).

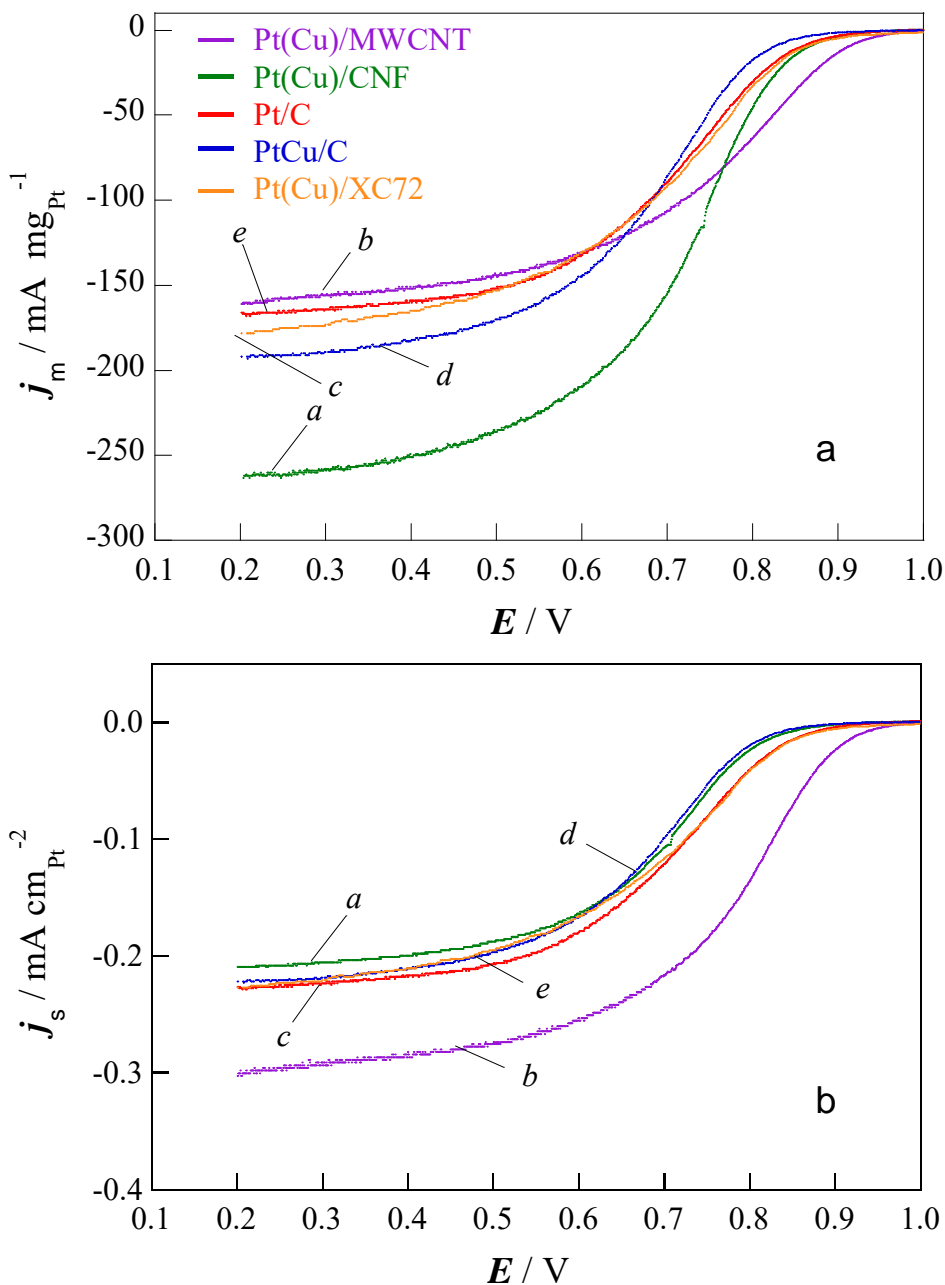


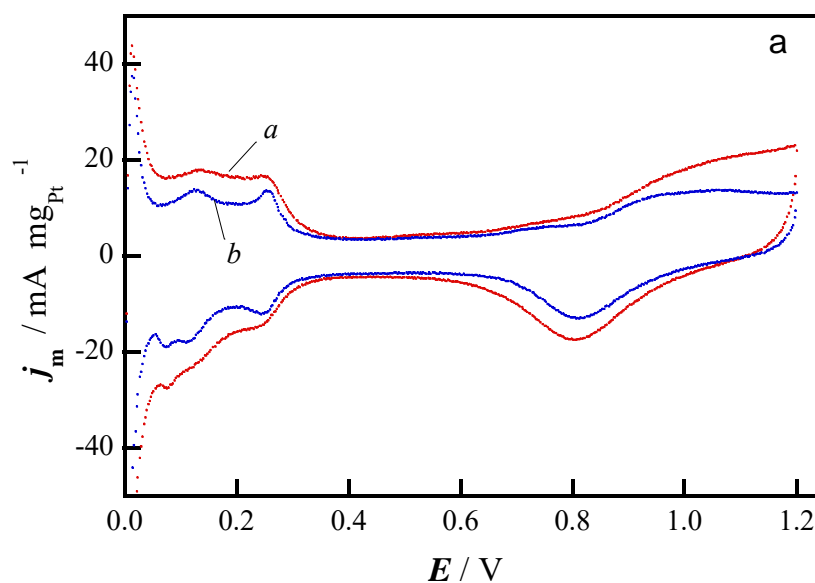
**Fig. 6** – Linear sweep voltammograms for oxygen reduction in  $\text{O}_2$ -saturated 0.50 M  $\text{H}_2\text{SO}_4$ , (a) considering the current per mass  $j_m$  and (b) the current per ECSA  $j_s$ , corresponding to Pt(Cu)/CNF (a), Pt(Cu)/MWCNT (b), Pt(Cu)/XC72 (c), PtCu/C (d) and Pt/C (e). Sweep rate:  $5 \text{ mV s}^{-1}$ . RDE rotation rate of 1500 rpm.

This behavior, which is very probably related to the catalyst-support interaction, merits to be further explored in depth. In fact, the specific activities  $j_s$  (currents referred to the ECSA) are more indicative of the electrocatalyst activity than the mass activities and current densities relative to the electrode section [49,50]. This is of particular interest when comparing electrocatalysts with nanoparticles having quite different size, as in our case. When the metal load and nanoparticle size are the same for different catalysts, it is expected that the surface specific activity at a given potential keeps the same order of magnitude as that of the current densities referred to the electrode section [50]. Then, both indicate their different electrocatalytic activity. For this reason, the  $j_s$  vs  $E$  plots, obtained dividing  $j_m$  by the corresponding ECSAs, have been depicted in Fig. 6b. As shown in this figure, Pt(Cu)/MWCNT not only presented the most positive onset potential but also the highest surface specific currents, being correlated to a greater electrocatalytic activity. Then, according to Fig. 6a and b, Pt(Cu)/CNF possessed higher mass activities than the others, but Pt(Cu)/MWCNT yielded greater specific activity. As the Pt(Cu) nanoparticles were prepared in the same manner, there must be a notable effect of the support on their behavior.

It is also of interest to analyze the relative stability of the synthesized catalysts. This can be done by continuously cycling the specimens between 0.0 and 1.2 V, from hydrogen adsorption to Pt and carbon oxidation [24], in deaerated 0.50 M H<sub>2</sub>SO<sub>4</sub>, employing a large number of cycles. The curves depicted in Fig. 7a, b and c show the initial cyclic voltammogram (curve *a*, *c*, *e*) using Pt(Cu)/CNF, Pt(Cu)/MWCNT and Pt(Cu)/XC72, respectively, in deaerated 0.5 M H<sub>2</sub>SO<sub>4</sub> at 20 mVs<sup>-1</sup> and the corresponding final cyclic voltammogram (curve *b*, *d*, *f*) at the same scan rate, obtained after 1000 cycles at 200 mV s<sup>-1</sup>. The occurrence of certain atomic restructuring can be inferred, which may result from the carbon and Pt oxidation with further Pt oxide reduction together with the local

restructuring and possible aggregation of the nanoparticles. After these tests, the final ECSAs were 53.1, 39.7 and 45.5  $\text{m}^2 \text{g}_{\text{Pt}}^{-1}$ , respectively, accounting for by ECSA losses of about 25%, 11% and 42%, respectively. These values are comparable to previous ones reported in the literature for somewhat different systems and protocols [40,41]. Thus, ECSA losses of 22% and 46% were reported for Pt nanoparticles deposited on MWCNTs (Pt/MWCNTs) and commercial Pt/C, respectively [41]. This confirms the much greater stability of the CNFs and the MWCNTs as compared to XC72. The greater loss in the case of Pt(Cu)/XC72 could then be related to its poorer corrosion resistance when compared with the CNFs and MWCNTs. The ECSA decrease for XC72 could be particularly enhanced by the rather spherical shape of the carbon particles (see Fig. 2e), which may stimulate the nanoparticle aggregation during carbon oxidation. In spite of undergoing an intermediate ECSA loss, the Pt(Cu)/CNF catalysts eventually exhibited the greatest ECSA.

Then, Pt(Cu)/CNF and Pt(Cu)/MWCNT, apart from presenting relatively good stability and contributing with high mass and specific activities, respectively, allow saving about 50% of Pt. These results suggest that they could be good candidates as cathodes for the ORR in low-temperature fuels cells.



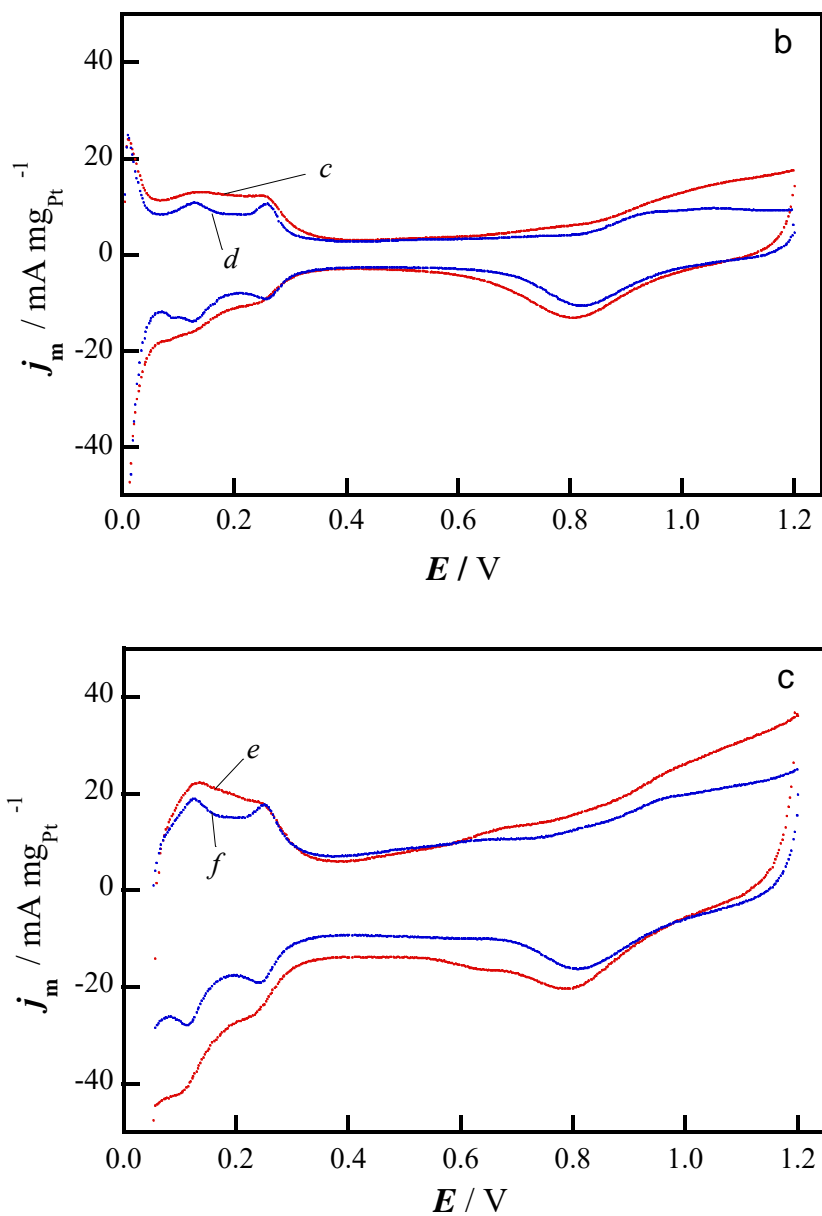


**Fig. 7** – Cyclic voltammograms of (a) Pt(Cu)/CNF, (b) Pt(Cu)/MWCNT and (c) Pt(Cu)/XC72 in deaerated 0.50 M H<sub>2</sub>SO<sub>4</sub> at 20 mV s<sup>-1</sup>, before the stability test (curves *a*, *c*, *e*) and after 1000 cycles within the same potential region at 200 mV s<sup>-1</sup> (curves *b*, *d*, *f*).

## 4. Conclusions

Pt(Cu) nanoparticle electrocatalysts, supported on CNFs, MWCNTs and Vulcan carbon XC72, were synthesized by electroless deposition of Cu and further galvanic exchange with  $\text{PtCl}_6^{2-}$ . The XRD analyses of Pt(Cu)/CNF, Pt(Cu)/MWCNT and Pt(Cu)/XC72 catalysts revealed Pt-like fcc structures with diffraction peaks between those corresponding to pure Pt and Cu, thus indicating the formation of a PtCu alloy. The mean crystallite sizes of the Pt(Cu) nanoparticles were about 3 nm. TEM observations revealed the carbon morphology of nanofibers, nanotubes and spherules along with a good dispersion and carbon attachment of the Pt(Cu) nanoparticles. The XPS analyses showed that the Pt(Cu) nanoparticles consisted of a PtCu alloy covered by a Pt-rich shell.

The ECSAs were determined from desorption of atomic hydrogen and also from CO stripping, yielding values of 70.5 and 78.5  $\text{m}^2 \text{g}_{\text{Pt}}^{-1}$  for Pt(Cu)/CNF and Pt(Cu)/XC72, respectively, which were comparable to those of commercial Pt/C and PtCu/C. A smaller value of 41.0  $\text{m}^2 \text{g}_{\text{Pt}}^{-1}$  was obtained for Pt(Cu)/MWCNT. The activation of the carbonaceous materials did not allow obtaining greater ECSAs. The carbon-supported Pt(Cu) catalysts showed onset potentials for CO oxidation about 50 mV more negative than those corresponding to Pt/C and PtCu/C, thus indicating the electronic effect of the Cu on Pt. This resulted in an easier CO oxidation and higher CO tolerance as compared to pure Pt.

The ORR curves obtained in  $\text{O}_2$ -saturated 0.50 M  $\text{H}_2\text{SO}_4$  using the RDE showed that the mass activity of Pt(Cu)/CNF was higher than that of commercial Pt/C and of PtCu/C, whereas those of Pt(Cu)/MWCNT and Pt(Cu)/XC72 were comparable to that of Pt/C. On the other hand, Pt(Cu)/MWCNT possessed higher specific activity than the others. According to the relative stability tests, Pt(Cu)/CNF and Pt(Cu)/MWCNT were

more resistant to corrosion and presented much smaller ECSA loss than Pt(Cu)/XC72. These results suggest that Pt(Cu)/CNF and Pt(Cu)/MWCNT could be suitable candidates for the ORR in the low-temperature fuel cells, eventually allowing a significant electrocatalyst cost decrease thanks to the 50 wt.% reduction in the amount of Pt employed.

## **Acknowledgments**

The authors thank the financial support from project CTQ2016-78616-R (AEI/FEDER, EU). The authors also thank the CCiT-UB (Scientific and Technological Centers of the Universitat de Barcelona) for the facilities in the electron microscope observations and the XRD and XPS analyses.

## References

- [1] Li W, Liu J, Zhao D. Mesoporous materials for energy conversion and storage devices. *Nat Rev Mater* 2016;1:16023. doi:10.1038/natrevmats.2016.23.
- [2] Daud WRW, Rosli RE, Majlan EH, Hamid SAA, Mohamed R, Husaini T. PEM fuel cell system control: a review. *Renew Energy* 2017;113:620–38. doi:10.1016/j.renene.2017.06.027.
- [3] Kamat P V. Meeting the clean energy demand: Nanostructure architectures for solar energy conversion. *J Phys Chem C* 2007;111:2834–60. doi:10.1021/jp066952u.
- [4] Sui S, Wang X, Zhou X, Su Y. A comprehensive review of Pt electrocatalysts for the oxygen reduction reaction: nanostructure, activity, mechanism and carbon support in PEM fuel. *J Mater Chem A* 2017;5:1808–25. doi:10.1039/c6ta08580f.
- [5] Wang Y, Chen KS, Mishler J, Cho SC, Adroher XC. A review of polymer electrolyte membrane fuel cells: rechnology, applications, and needs on fundamental research. *Appl Energy* 2011;88:981–1007. doi:10.1016/j.apenergy.2010.09.030.
- [6] Ruth K, Vogt M, Zuber R. Development of CO-tolerant catalysts on Pt/Ru catalysts. In: Vielstich W, Gasteiger HA, Lamm A, editors. *Handb. Fuel Cells - Fundam. Technol. Appl.*, New York: John Wiley & Sons; 2010, pp. 489–96.
- [7] Velázquez-Palenzuela A, Brillas E, Arias C, Centellas F, Garrido JA, Rodríguez RM, Cabot PL. Structural analysis of carbon-supported Ru-decorated Pt nanoparticles synthesized using forced deposition and catalytic performance toward CO, methanol, and ethanol electro-oxidation. *J Catal* 2013;298:112–21. doi:10.1016/j.jcat.2012.11.006.
- [8] Antolini E. Formation of carbon-supported PtM alloys for low temperature fuel

- cells : a review. *Mater Chem Phys* 2003;78:563–73.  
doi:[https://doi.org/10.1016/S0254-0584\(02\)00389-9](https://doi.org/10.1016/S0254-0584(02)00389-9).
- [9] Liu Z, Ling XY, Su X, Lee JY. Carbon-supported Pt and PtRu nanoparticles as catalysts for a direct methanol fuel cell. *J Phys Chem B* 2004;108:8234–40. doi:10.1021/jp049422b.
- [10] Shao M, Sasaki K, Nebojsa MS, Zhang L, Adzic RR. Synthesis and characterization of platinum monolayer oxygen-reduction electrocatalysts with Co–Pd core–shell nanoparticle supports. *Electrochem Commun* 2007;9:2848–53. doi:10.1016/j.elecom.2007.10.009.
- [11] Papadimitriou S, Tegou A, Pavlidou E, Armanyanov S, Valova E, Kokkinidis G, Sotiropoulos S. Preparation and characterisation of platinum- and gold-coated copper, iron, cobalt and nickel deposits on glassy carbon substrates. *Electrochim Acta* 2008;53:6559–67. doi:10.1016/j.electacta.2008.04.015.
- [12] Mohl M, Dobo D, Kukovecz A, Konya Z, Kordas K, Wei J, Vajtai R, Ajayan PM. Formation of CuPd and CuPt bimetallic nanotubes by galvanic replacement reaction. *J Phys Chem C* 2011;115:9403–9. doi:10.1021/jp112128g.
- [13] Xia BY, Wu H Bin, Wang X, Wen X, Lou D. One-pot synthesis of cubic PtCu<sub>3</sub> nanocages with enhanced electrocatalytic activity for the methanol oxidation reaction. *J Am Chem Soc* 2012;134:13934–7. doi:10.1021/ja3051662.
- [14] Xiong L, Manthiram A. Effect of atomic ordering on the catalytic activity of carbon supported PtM ( M = Fe , Co , Ni , and Cu ) alloys for oxygen reduction in PEMFCs 2005. *J Electrochem Soc* 2005; 152:A697–703. doi:10.1149/1.1862256.
- [15] Oezaslan M, Strasser P. Activity of dealloyed PtCo<sub>3</sub> and PtCu<sub>3</sub> nanoparticle electrocatalyst for oxygen reduction reaction in polymer electrolyte membrane fuel cell. *J Power Sources* 2011;196:5240–9. doi:10.1016/j.jpowsour.2010.11.016.

- [16] Oezaslan M, Strasser P. PtCu<sub>3</sub>, PtCu and Pt<sub>3</sub>Cu alloy nanoparticle electrocatalysts for oxygen reduction reaction in alkaline and acidic medium. *J Electrochem Soc* 2012;159:B444–54. doi:10.1149/2.106204jes.
- [17] Jayasayee K, Rob van Veen JA, Manivasagam TG, Celebi S, Hensen EJM, de Bruijn FA. Oxygen reduction reaction (ORR) activity and durability of carbon supported PtM (Co, Ni, Cu) alloys : influence of particle size and non-noble metals. *Appl Catal B: Environ* 2012;111–112:515–26. doi:10.1016/j.apcatb.2011.11.003.
- [18] Caballero-Manrique G, Velázquez-Palenzuela A, Brillas E, Centellas F, Garrido JA, Rodríguez RM, Cabot PL. Electrochemical synthesis and characterization of carbon-supported Pt and Pt-Ru nanoparticles with Cu cores for CO and methanol oxidation in polymer electrolyte fuel cells. *Int J Hydrogen Energy* 2014;39:12859–69. doi:10.1016/j.ijhydene.2014.06.089.
- [19] Mintsouli I, Georgieva J, Armyanov S, Valova E, Avdeev G, Hubin A, Steenhaut O, Dille J, Tsiplakides D, Balomenou S, Sotiropoulos S. Pt-Cu electrocatalysts for methanol oxidation prepared by partial galvanic replacement of Cu/carbon powder precursors. *Appl Catal B: Environ* 2013;136–137:160–7. doi:10.1016/j.apcatb.2013.01.059.
- [20] Guterman VE, Belenov S V, Alekseenko AA, Lin R, Tabachkova NY, Safronenko OI. Activity and stability of Pt/C and Pt-Cu/C electrocatalysts. *Electrocatalysis* 2018;9:550–62.
- [21] Sarkar A, Manthiram A. Synthesis of Pt@Cu core-shell nanoparticles by galvanic displacement of Cu by Pt<sup>4+</sup> ions and their application as electrocatalysts for oxygen reduction reaction in fuel cells. *J Phys Chem C* 2010;114:4725–32. doi:10.1021/jp908933r.
- [22] Podlovchenko BI, Gladysheva TD, Filatov AY, Yashina LV. The use of galvanic

- displacement in synthesizing Pt(Cu) catalysts with the core-shell structure. *Russ J Electrochem* 2010;46:1189–97. doi:10.1134/S1023193510100150.
- [23] Caballero-Manrique G, Nadeem I, Brillas E, Centellas F, Garrido J, Rodríguez RM, Cabot, PL. Effects of the electrodeposition time in the synthesis of carbon-supported Pt(Cu) and Pt-Ru(Cu) core-shell electrocatalysts for polymer electrolyte fuel cells. *Catalysts* 2016;6:125–42. doi:10.3390/catal6080125.
- [24] Caballero-Manrique G, Brillas E, Centellas F, Garrido JA, Rodríguez RM, Cabot PL. Electrochemical oxidation of the carbon support to synthesize Pt(Cu) and Pt-Ru(Cu) core-shell electrocatalysts for low-temperature fuel cells. *Catalysts* 2015;5:815–37. doi:10.3390/catal5020815.
- [25] Geboes B, Mintsouli I, Wouters B, Georgieva J, Kakaroglou A, Sotiropoulos S, Valova E, Armyanov S, Hubin A, Breugelmans T. Surface and electrochemical characterisation of a Pt-Cu/C nano-structured electrocatalyst, prepared by galvanic displacement. *Appl Catal B: Environ* 2014;150–151:249–56. doi:10.1016/j.apcatb.2013.12.020.
- [26] Georgieva J, Valova E, Mintsouli I, Sotiropoulos S, Armyanov S, Kakaroglou A, Hubin A, Steenhaut O, Dille J. Carbon-supported Pt(Cu) electrocatalysts for methanol oxidation prepared by Cu electroless deposition and its galvanic replacement by Pt. *J Appl Electrochem* 2014;44:215–24. doi:10.1007/s10800-013-0618-2.
- [27] Pryadchenko VV, Srabionyan VV, Kurzin AA, Bulat NV, Shemet DB, Avakyan LA, Belenov SV, Volochaev VA, Zizak I, Guterman VE, Bugaev LA. Bimetallic PtCu core-shell nanoparticles in PtCu/C electrocatalysts: structural and electrochemical characterization. *Appl Catal A: Gen* 2016;525:226–36. doi:10.1016/j.apcata.2016.08.008.

- [28] Alekseenko AA, Belenov SV, Menshikov VS, Guterman VE. Pt(Cu)/C Electrocatalysts with low platinum content. *Russ J Electrochem* 2018;54:415–25. doi:10.1134/S1023193518050026.
- [29] Alekseenko AA, Guterman VE, Belenov S V., Menshikov VS, Tabachkova NY, Safronenko OI, Moguchikh EA. Pt/C electrocatalysts based on the nanoparticles with the gradient structure. *Int J Hydrogen Energy* 2018;43:3676–87. doi:10.1016/j.ijhydene.2017.12.143.
- [31] Maya-Cornejo J, Carrera-Cerritos R, Sebastián D, Ledesma-García J, Arriaga LG, Aricò AS, Baglio V. PtCu catalyst for the electro-oxidation of ethanol in an alkaline direct alcohol fuel cell. *Int J Hydrogen Energy* 2017;42:27919–28. doi: 10.1016/j.ijhydene.2017.07.226.
- [32] Pryadchenko VV, Belenov SV, Shemet DB, Srabionyan VV, Avakyan LA, Volochaev VA, Mikheykin AS, Bdoyan KE, Zizak I, Guterman VE, Bugaev LA. Effect of Thermal Treatment on the Atomic Structure and Electrochemical Characteristics of Bimetallic PtCu Core–Shell Nanoparticles in PtCu/C Electrocatalysts. *J Phys Chem C* 2018;122:17199–210. doi: 10.1021/acs.jpcc.8b03696.
- [33] Sung Y, Hwang J, Shik J. Characterization and activity correlations of Pt bimetallic catalysts for low temperature fuel cells. *Int J Hydrogen Energy* 2011;36:4007–14. <http://dx.doi.org/10.1016/j.ijhydene.2010.12.058>.
- [34] Xu Z, Zhang H, Liu S, Zhang B, Zhong H. Facile synthesis of supported Pt-Cu nanoparticles with surface enriched Pt as highly active cathode catalyst for proton exchange membrane fuel cells. *Int J Hydrogen Energy* 2012;37:17978–83. doi:10.1016/j.ijhydene.2012.09.050.
- [35] Yang L, Ding Y, Chen L, Luo S. Hierarchical reduced graphene oxide supported

- dealloyed platinum e copper nanoparticles for highly efficient methanol electrooxidation. *Int J Hydrogen Energy* 2017;42:6705–12. doi:10.1016/j.ijhydene.2017.01.133.
- [36] Hoseini SJ, Bahrami M, Samadi Z, Hashemi SF, Roushani M, Habib B. Designing of some platinum or palladium-based nanoalloys as effective electrocatalysts for methanol oxidation reaction. *Int J Hydrogen Energy* 2018;43:15095–111. doi:10.1016/j.ijhydene.2018.06.062.
- [30] Guterman VE, Lastovina TA, Belenov S V., Tabachkova NY, Vlasenko VG, Khodos II, Balakshina EN. PtM/C (M=Ni, Cu, or Ag) electrocatalysts: Effects of alloying components on morphology and electrochemically active surface areas. *J Solid State Electrochem* 2014;18:1307–17. doi:10.1007/s10008-013-2314-x.
- [37] Sharma S, Pollet BG. Support materials for PEMFC and DMFC electrocatalysts - A review. *J Power Sources* 2012;208:96–119. doi:10.1016/j.jpowsour.2012.02.011.
- [38] Shao Y, Liu J, Wang Y, Lin Y. Novel catalyst support materials for PEM fuel cells: Current status and future prospects. *J Mater Chem* 2009;19:46–59. doi:10.1039/b808370c.
- [39] Stobinski L, Lesiak B, Kövér L, Tóth J, Biniak S, Trykowski G, Judek J. Multiwall carbon nanotubes purification and oxidation by nitric acid studied by the FTIR and electron spectroscopy methods. *J Alloys Compd* 2010;501:77–84. doi:10.1016/j.jallcom.2010.04.032.
- [40] Shao Y, Yin G, Gao Y, Shi P. Durability Study of Pt/C and Pt/CNTs catalysts under simulated PEM fuel cell conditions. *J Electrochem Soc* 2006;153:A1093–7. doi:10.1149/1.2191147.
- [41] Devrim Y, Arica ED. Multi-walled carbon nanotubes decorated by platinum

- catalyst for high temperature PEM fuel cell. *Int J Hydrogen Energy* 2019;44:18951–66. doi:10.1016/j.ijhydene.2019.01.051.
- [42] El-Deeb H, Bron M. Microwave-assisted polyol synthesis of PtCu/carbon nanotube catalysts for electrocatalytic oxygen reduction. *J Power Sources* 2015;275:893–900. doi:10.1016/j.jpowsour.2014.11.060.
- [43] El-Deeb H, Bron M. Electrochemical dealloying of PtCu/CNT electrocatalysts synthesized by NaBH<sub>4</sub>-assisted polyol-reduction: influence of preparation parameters on oxygen reduction activity. *Electrochim Acta* 2015;164:315–22. doi:10.1016/j.electacta.2015.02.137.
- [44] Rivera-Lugo YY, Salazar-Gastélum MI, López-Rosas DM, Reynoso-Soto EA, Pérez-Sicairos S, Velraj S, Flores-Hernández JR, Félix-Navarro RM. Effect of template, reaction time and platinum concentration in the synthesis of PtCu/CNT catalyst for PEMFC applications. *Energy* 2018;148:561–70. doi:10.1016/j.energy.2018.01.069.
- [45] Powder Diffraction File (2018). International Centre for Diffraction Data (ICDD), 12 Campus Boulevard., Newton Square, Pennsylvania 19073-3273, USA. n.d. <http://www.icdd.com>. Accessed: september 2019.
- [46] Esparbé I, Brillas E, Centellas F, Garrido JA, Rodríguez RM, Arias C, Cabot PL. Structure and electrocatalytic performance of carbon-supported platinum nanoparticles. *J Power Sources* 2009;190:201–9. doi:10.1016/j.jpowsour.2009.01.075.
- [47] Serrano-Ruiz JC, López-Cudero A, Solla-Gullón J, Sepúlveda-Escribano A, Aldaz A, Rodríguez-Reinoso F. Hydrogenation of  $\alpha,\beta$  unsaturated aldehydes over polycrystalline, (111) and (100) preferentially oriented Pt nanoparticles supported on carbon. *J Catal* 2008;253:159–66. doi:10.1016/j.jcat.2007.10.010.

- [48] Kitchin JR, Barteau MA. Modification of the surface electronic and chemical properties of Pt (111) by subsurface 3d transition metals. *J Chem Phys* 2014;120:10240–6. doi:10.1063/1.1737365.
- [49] Cui C, Gan L, Li HH, Yu SH, Heggen M, Strasser P. Octahedral PtNi nanoparticle catalysts: exceptional oxygen reduction activity by tuning the alloy particle surface composition. *Nano Lett* 2012;12:5885–9. doi: dx.doi.org/10.1021/nl3032795.
- [50] Beerman V, Gocyla M, Willinger E, Rudi S, Heggen M, Dunin-Borkowski RE, Willinger MG, Strasser P. Rh-doped Pt-Ni octahedral nanoparticles: understanding the correlation between elemental distribution, ORR and shape stability. *Nano Lett* 2016;16:1719–25. doi: 10.1021/acs.nanolett.5b04636.